

Modern Physics Letters A  
 © World Scientific Publishing Company

## Sum Rules and Moments of the Nucleon Spin Structure Functions

J.-P. Chen, A. Deur

*Thomas Jefferson National Accelerator Facility  
 12000 Jefferson Avenue, Newport News, Virginia 23606, USA  
 jpchen@jlab.org*

Z.-E. Meziani

*Department of Physics, Temple University  
 Philadelphia, Pennsylvania 19122, USA*

Received ()

The nucleon has been used as a laboratory to investigate its own spin structure and Quantum Chromodynamics. New experimental data on nucleon spin structure at low to intermediate momentum transfers combined with existing high momentum transfer data offer a comprehensive picture of the transition region from the *confinement* regime of the theory to its *asymptotic freedom* regime. Insight for some aspects of the theory is gained by exploring lower moments of spin structure functions and their corresponding sum rules (i.e. the Gerasimov-Drell-Hearn, Bjorken and Burkhardt-Cottingham). These moments are expressed in terms of an operator-product expansion using quark and gluon degrees of freedom at moderately large momentum transfers. The sum rules are verified to good accuracy assuming that no singular behavior of the structure functions is present at very high excitation energies. The higher-twist contributions have been examined through the moments evolution as the momentum transfer varies from higher to lower values. Furthermore, QCD-inspired low-energy effective theories, which explicitly include chiral symmetry breaking, are tested at low momentum transfers. The validity of these theories is further examined as the momentum transfer increases to moderate values. It is found that chiral perturbation calculations agree reasonably well with the first moment of the spin structure function  $g_1$  at momentum transfer of  $0.1 \text{ GeV}^2$  but fail to reproduce the neutron data in the case of the generalized polarizability  $\delta_{LT}$ .

*Keywords:* Nucleon; Spin; Sum Rule; Moment; QCD; Higher Twist; Jefferson Lab.

### 1. Introduction

In the last twenty-five years the spin structure of the nucleon led to a very productive experimental and theoretical activity with exciting results and new challenges<sup>1</sup>. This investigation has included a variety of aspects, such as testing Quantum Chromodynamics (QCD), the theory of strong interactions, in its perturbative regime *via* spin sum rules (like the Bjorken sum rule<sup>2</sup>) and understanding how the spin of the nucleon is built from the intrinsic degrees of freedom of the theory, quarks and gluons. Recently, results from a new generation of experiments performed at Jefferson Lab seeking to probe the theory in its non-perturbative and transition regimes

2 *J.-P. Chen, A. Deur and Z.-E. Meziani*

have reached a mature state. The low momentum-transfer results offer insight in a region known for the collective behavior of the nucleon constituents and their interactions. In this region it has been more economical to describe the nucleon using effective degrees of freedom like mesons and constituent quarks rather than current quarks and gluons. Furthermore, distinct features seen in the nucleon response to the electromagnetic probe, depending on the resolution of the probe, point clearly to different regimes of description, i.e. a scaling regime where quark-gluon correlations are suppressed versus a coherent regime where long-range interactions give rise to the static properties of the nucleon.

In this review we describe an investigation<sup>3,4,5,6,7,8,9,10,11</sup> of the spin structure of the nucleon through the measurement of the helicity-dependent photoabsorption cross sections or asymmetries using virtual photons across a wide resolution spectrum. These observables are used to extract the spin structure functions  $g_1$  and  $g_2$  and evaluate their moments. These moments are powerful tools to test QCD sum rules and unravel some aspects of the quark-gluon structure of the nucleon.

## 2. Sum rules and Moments

Sum rules involving the spin structure of the nucleon offer an important opportunity to study QCD. In recent years the Bjorken sum rule at large  $Q^2$  (4-momentum transfer squared) and the Gerasimov, Drell and Hearn (GDH) sum rule<sup>12,13</sup> at  $Q^2 = 0$  have attracted large experimental<sup>14,15,16</sup> and theoretical<sup>17</sup> efforts that have provided us with rich information. This first type of sum rules relates the moments of the spin structure functions (or, equivalently, the spin-dependent total photoabsorption cross sections) to the nucleon's static properties. The second type of sum rules, such as the generalized GDH sum rule<sup>18,19</sup> or the polarizability sum rules<sup>20,21</sup>, relate the moments of the spin structure functions to real or virtual Compton amplitudes, which can be calculated theoretically. Both types of sum rules are based on "unsubtracted" dispersion relations and the optical theorem<sup>22</sup>. The first type of sum rules uses one more general assumption, such as a low-energy theorem<sup>23</sup> for the GDH sum rule and Operator Production Expansion (OPE)<sup>24</sup> for the Bjorken sum rule, to relate the Compton amplitude to a static property.

The formulation below follows closely Ref. <sup>20,21</sup>. Consider the forward doubly-virtual Compton scattering (VVCS) of a virtual photon with space-like four-momentum  $q$ , i.e.,  $q^2 = \nu^2 - \vec{q}^2 = -Q^2 < 0$ , where  $\nu$  is the energy and  $\vec{q}$  is the three momentum of the virtual photon. The absorption of a virtual photon on a nucleon is related to inclusive electron scattering. The inclusive cross section, assuming parity conservation, contains four partial cross sections (or structure functions):  $\sigma_T$ ,  $\sigma_L$ ,  $\sigma_{TT}$ ,  $\sigma_{LT}$ , (or  $F_1$ ,  $F_2$ ,  $g_1$ ,  $g_2$ ). The first two are spin-averaged, while the last two are spin-dependent. In this review, we will concentrate on the spin-dependent ones. In the following discussion, we will start with the general situation, i.e., sum rules valid for all  $Q^2$ , then discuss the two limiting cases at low  $Q^2$  and at high  $Q^2$ .

Considering the spin-flip VVCS amplitude  $g_{TT}$  and assuming it has an appropri-

ate convergence behavior at high energy, an unsubtracted dispersion relation leads to the following equation for  $g_{TT}$ :

$$\text{Re}[g_{TT}(\nu, Q^2) - g_{TT}^{pole}(\nu, Q^2)] = \left(\frac{\nu}{2\pi^2}\right) \mathcal{P} \int_{\nu_0}^{\infty} \frac{K(\nu', Q^2) \sigma_{TT}(\nu', Q^2)}{\nu'^2 - \nu^2} d\nu', \quad (1)$$

where  $g_{TT}^{pole}$  is the nucleon pole (elastic) contribution,  $\mathcal{P}$  denotes the principal value integral and  $K$  is the virtual photon flux factor. The lower limit of the integration  $\nu_0$  is the pion-production threshold on the nucleon. A low-energy expansion gives:

$$\text{Re}[g_{TT}(\nu, Q^2) - g_{TT}^{pole}(\nu, Q^2)] = \left(\frac{2\alpha}{M^2}\right) I_{TT}(Q^2) \nu + \gamma_{TT}(Q^2) \nu^3 + O(\nu^5), \quad (2)$$

with  $\alpha$  the electromagnetic fine-structure constant and  $M$  the nucleon mass.  $I_{TT}(Q^2)$  is the coefficient of the  $O(\nu)$  term of the Compton amplitude. Equation (2) defines the generalized forward spin polarizability  $\gamma_{TT}(Q^2)$  (or  $\gamma_0(Q^2)$  as it was used in Refs. <sup>5,20</sup>). Combining Eqs. (1) and (2), the  $O(\nu)$  term yields a sum rule for the generalized GDH integral<sup>17,18</sup>:

$$\begin{aligned} I_{TT}(Q^2) &= \frac{M^2}{4\pi^2\alpha} \int_{\nu_0}^{\infty} \frac{K(\nu, Q^2)}{\nu} \frac{\sigma_{TT}}{\nu} d\nu \\ &= \frac{2M^2}{Q^2} \int_0^{x_0} \left[ g_1(x, Q^2) - \frac{4M^2}{Q^2} x^2 g_2(x, Q^2) \right] dx \end{aligned} \quad (3)$$

where  $x = Q^2/2M\nu$  is the Bjorken scaling variable. As  $Q^2 \rightarrow 0$ , the low-energy theorem relates  $I(0)$  to the anomalous magnetic moment of the nucleon,  $\kappa$ , and Eq. (3) becomes the original GDH sum rule<sup>12,13</sup>:

$$I(0) = \int_{\nu_0}^{\infty} \frac{\sigma_{1/2}(\nu) - \sigma_{3/2}(\nu)}{\nu} d\nu = -\frac{2\pi^2\alpha\kappa^2}{M^2}, \quad (4)$$

where  $\sigma_{1/2(3/2)}$  is the total photoabsorption cross section with a projection of  $\frac{1}{2}$  ( $\frac{3}{2}$ ) for the total spin along the direction of photon momentum, and  $2\sigma_{TT} \equiv \sigma_{1/2} - \sigma_{3/2}$ . The  $O(\nu^3)$  term yields a sum rule for the generalized forward spin polarizability<sup>20,21</sup>:

$$\begin{aligned} \gamma_{TT}(Q^2) &= \left(\frac{1}{2\pi^2}\right) \int_{\nu_0}^{\infty} \frac{K(\nu, Q^2)}{\nu} \frac{\sigma_{TT}(\nu, Q^2)}{\nu^3} d\nu \\ &= \frac{16\alpha M^2}{Q^6} \int_0^{x_0} x^2 \left[ g_1(x, Q^2) - \frac{4M^2}{Q^2} x^2 g_2(x, Q^2) \right] dx. \end{aligned} \quad (5)$$

Considering the longitudinal-transverse interference amplitude  $g_{LT}$ , with the same assumptions, one obtains:

$$\text{Re}[g_{LT}(\nu, Q^2) - g_{LT}^{pole}(\nu, Q^2)] = \left(\frac{2\alpha}{M^2}\right) Q I_{LT}(Q^2) + Q \delta_{LT}(Q^2) \nu^2 + O(\nu^4) \quad (6)$$

where the  $O(1)$  term leads to a sum rule for  $I_{LT}(Q^2)$ , which relates it to the  $\sigma_{LT}$  integral over the excitation spectrum.

$$I_{LT}(Q^2) = \frac{M^2}{4\pi^2\alpha} \int_{\nu_0}^{\infty} \frac{K(\nu, Q^2)}{\nu} \frac{\sigma_{LT}(\nu, Q^2)}{Q} d\nu$$

4 *J.-P. Chen, A. Deur and Z.-E. Meiziani*

$$= \frac{2M^2}{Q^2} \int_0^{x_0} x^2 [g_1(x, Q^2) + g_2(x, Q^2)] dx. \quad (7)$$

The  $O(\nu^2)$  term leads to the generalized longitudinal-transverse polarizability<sup>20,21</sup>:

$$\begin{aligned} \delta_{LT}(Q^2) &= \left(\frac{1}{2\pi^2}\right) \int_{\nu_0}^{\infty} \frac{K(\nu, Q^2)}{\nu} \frac{\sigma_{LT}(\nu, Q^2)}{Q\nu^2} d\nu \\ &= \frac{16\alpha M^2}{Q^6} \int_0^{x_0} x^2 [g_1(x, Q^2) + g_2(x, Q^2)] dx. \end{aligned} \quad (8)$$

Alternatively, we can consider the covariant spin-dependent VVCS amplitudes  $S_1$  and  $S_2$ , which are related to the spin-flip amplitudes  $g_{TT}$  and  $g_{LT}$ :

$$S_1(\nu, Q^2) = \frac{\nu M}{\nu^2 + Q^2} \left[ g_{TT}(\nu, Q^2) + \frac{Q}{\nu} g_{LT}(\nu, Q^2) \right], \quad (9)$$

$$S_2(\nu, Q^2) = -\frac{M^2}{\nu^2 + Q^2} \left[ g_{TT}(\nu, Q^2) - \frac{\nu}{Q} g_{LT}(\nu, Q^2) \right]. \quad (10)$$

Dispersion relation with the same assumptions leads to

$$\text{Re}[S_1(\nu, Q^2) - S_1^{pole}(\nu, Q^2)] = \frac{4\alpha}{M} I_1(Q^2) + \gamma_{g_1}(Q^2)\nu^2 + O(\nu^4), \quad (11)$$

where the  $O(1)$  term leads to a sum rule for  $I_1(Q^2)$ :

$$I_1(Q^2) = \frac{2M^2}{Q^2} \int_0^{x_0} g_1(x, Q^2) dx. \quad (12)$$

The  $O(\nu^2)$  term leads to the generalized  $g_1$  polarizability:

$$\begin{aligned} \gamma_{g_1}(Q^2) &= \frac{16\pi\alpha M^2}{Q^6} \int_0^{x_0} x^2 g_1(x, Q^2) dx \\ &= \delta_{LT} + \frac{2\alpha}{M^2 Q^2} (I_{TT}(Q^2) - I_1(Q^2)). \end{aligned} \quad (13)$$

For  $S_2$ , assuming a Regge behavior at  $\nu \rightarrow \infty$  given by  $S_2 \rightarrow \nu^{\alpha_2}$  with  $\alpha_2 < -1$ , the unsubtracted dispersion relations for  $S_2$  and  $\nu S_2$ , without the elastic pole subtraction, lead to a ‘‘super-convergence relation’’ that is valid for any value of  $Q^2$ ,

$$\int_0^1 g_2(x, Q^2) dx = 0, \quad (14)$$

which is the Burkhardt-Cottingham (BC) sum rule<sup>25</sup>. It can also be written as

$$I_2(Q^2) = \frac{2M^2}{Q^2} \int_0^{x_0} g_2(x, Q^2) dx = \frac{1}{4} F_P(Q^2) (F_D(Q^2) + F_P(Q^2)), \quad (15)$$

where  $F_P$  and  $F_D$  are the Pauli and Dirac form factors for elastic e-N scattering.

The low-energy expansion of the dispersion relation leads to

$$\begin{aligned} &\text{Re} [(\nu S_2(\nu, Q^2)) - (\nu S_2^{pole}(\nu, Q^2))] \\ &= 2\alpha I_2(Q^2) - \frac{2\alpha}{Q^2} (I_{TT}(Q^2) - I_1(Q^2))\nu^2 + \frac{M^2}{Q^2} \gamma_{g_2}(Q^2)\nu^4 + O(\nu^6), \end{aligned} \quad (16)$$

where the  $O(\nu^4)$  term gives the generalized  $g_2$  polarizability:

$$\begin{aligned}\gamma_{g_2}(Q^2) &= \frac{16\pi\alpha M^2}{Q^6} \int_0^{x_0} x^2 g_2(x, Q^2) dx \\ &= \delta_{LT}(Q^2) - \gamma_{TT}(Q^2) + \frac{2\alpha}{M^2 Q^2} (I_{TT}(Q^2) - I_1(Q^2)).\end{aligned}\quad (17)$$

At high  $Q^2$ , the OPE<sup>27,28,29</sup> for the VVCS amplitude leads to the twist expansion:

$$\Gamma_1(Q^2) \equiv \int_0^1 g_1(x, Q^2) dx = \sum_{\tau=2,4,\dots} \frac{\mu_\tau(Q^2)}{(Q^2)^{(\tau-2)/2}} \quad (18)$$

with the coefficients  $\mu_\tau$  related to nucleon matrix elements of operators of twist  $\leq \tau$ . Here twist is defined as the mass dimension minus the spin of an operator and  $\mu_\tau$  itself is a perturbative series in  $\alpha_s$ , the effective strong coupling constant. Note that the application of the OPE requires summation over all hadronic final states, including the elastic at  $x = 1$ .

The leading-twist (twist-2) component,  $\mu_2$ , is determined by matrix elements of the axial vector operator  $\bar{\psi}\gamma_\mu\gamma_5\psi$ , summed over quark flavors, where  $\psi$  are the quark field operators. It can be decomposed into flavor triplet ( $g_A$ ), octet ( $a_8$ ) and singlet ( $\Delta\Sigma$ ) axial charges,

$$\mu_2(Q^2) = \left( \pm \frac{1}{12} g_A + \frac{1}{36} a_8 \right) + \frac{1}{9} \Delta\Sigma + O(\alpha_s(Q^2)), \quad (19)$$

where +(-) corresponds to proton (neutron) and the  $O(\alpha_s)$  terms are the  $Q^2$  evolution due to the QCD radiative effects that can be calculated from perturbative QCD. The triplet axial charge is obtained from neutron  $\beta$ -decay, while the octet axial charge can be extracted from hyperon weak-decay matrix elements assuming SU(3) flavor symmetry. Within the quark-parton model  $\Delta\Sigma$  is the amount of nucleon spin carried by the quarks. Deep Inelastic Scattering (DIS) experiments at large  $Q^2$  have extracted this quantity through a global analysis of the world data<sup>1</sup>.

Eqs. (18) and (19), at leading twist, lead to the Ellis-Jaffe sum rule<sup>26</sup> with the assumptions of SU(3) flavor symmetry and an unpolarized strange sea. The difference between the proton and the neutron gives the flavor non-singlet term:

$$\Gamma_1^p(Q^2) - \Gamma_1^n(Q^2) = \frac{1}{6} g_A + O(\alpha_s) + O(1/Q^2), \quad (20)$$

which becomes the Bjorken sum rule at the  $Q^2 \rightarrow \infty$  limit.

If the nucleon mass were zero,  $\mu_\tau$  would contain only a twist- $\tau$  operator. The non-zero nucleon mass induces contributions to  $\mu_\tau$  from lower-twist operators. The twist-4 term contains a twist-2 contribution,  $a_2$ , and a twist-3 contribution,  $d_2$ , in addition to  $f_2$ , the twist-4 component<sup>27,28,29,30</sup>:

$$\mu_4 = M^2 (a_2 + 4d_2 + 4f_2) / 9. \quad (21)$$

6 *J.-P. Chen, A. Deur and Z.-E. Meiziani*

The twist-2 matrix element  $a_2$  is:

$$a_2 S^{\{\mu} P^\nu P^{\lambda\}} = \frac{1}{2} \sum_q e_q^2 \langle P, S | \bar{\psi}_q \gamma^{\{\mu} i D^\nu i D^{\lambda\}} \psi_q | P, S \rangle, \quad (22)$$

where  $e_q$  is the electric charge of a quark with flavor  $q$ ,  $S$  and  $P$  are the covariant spin and momentum vectors,  $D^\nu$  are the covariant derivatives, and the parentheses  $\{\cdot\cdot\}$  denote symmetrization of indices. The matrix element  $a_2$  is related to the second moment of the twist-2 part of  $g_1$ :

$$a_2(Q^2) = 2 \int_0^1 dx x^2 g_1(x, Q^2). \quad (23)$$

Taking Eq. (23) as the definition of  $a_2$ , it is now generalized to any  $Q^2$ , including twist-2 and higher-twist contributions. At low  $Q^2$ , the inelastic part of  $a_2$ , is related to  $\gamma_{g_1}$ , the generalized  $g_1$  polarizability:

$$\bar{a}_2(Q^2) = \frac{Q^6}{8\pi\alpha M^3} \gamma_{g_1}. \quad (24)$$

Note that at large  $Q^2$ , the elastic contribution is negligible and  $\bar{a}_2$  becomes  $a_2$ .

The twist-3 component,  $d_2$ , is defined by the matrix element<sup>27,28,29,30</sup>:

$$d_2 S^{\{\mu} P^{\{\nu} P^{\lambda\}} = \frac{1}{8} \sum_q \langle P, S | \bar{\psi}_q g \bar{F}^{\{\mu\nu} \gamma^{\lambda\}} \psi_q | P, S \rangle, \quad (25)$$

where  $g$  is the QCD coupling constant,  $\bar{F}^{\mu\nu} = (1/2)e^{\mu\nu\alpha\beta} F_{\alpha\beta}$ ,  $F_{\alpha\beta}$  are the gluon field operators, and the parentheses  $[\cdot\cdot]$  denote antisymmetrization of indices. This matrix element is related to the second moments of the twist-3 part of  $g_1$  and  $g_2$ :

$$\begin{aligned} d_2(Q^2) &= \int_0^1 dx x^2 (2g_1(x, Q^2) + 3g_2(x, Q^2)) \\ &= 3 \int_0^1 dx x^2 (g_2(x, Q^2) - g_2^{WW}(x, Q^2)), \end{aligned} \quad (26)$$

where  $g_2^{WW}$  is the twist-2 part of  $g_2$  as derived by Wandzura and Wilczek<sup>31</sup>

$$g_2^{WW}(x, Q^2) = g_1(x, Q^2) + \int_x^1 dy \frac{g_1(y, Q^2)}{y}. \quad (27)$$

The definition of  $d_2$  with Eq. (26) is generalized to all  $Q^2$ . At low  $Q^2$ , the inelastic part of  $d_2(Q^2)$  is related to the polarizabilities:

$$\bar{d}_2(Q^2) = \frac{8\pi\alpha M^3}{Q^6} (\gamma_{g_1} + \frac{3}{2} \gamma_{g_2}) = \frac{Q^4}{8M^4} (I_1(Q^2) - I_{TT}(Q^2) + \frac{M^2 Q^2}{\alpha} \delta_{LT}(Q^2)). \quad (28)$$

At large  $Q^2$ ,  $\bar{d}_2$  becomes  $d_2$  since the elastic contribution becomes negligible.

The twist-4 contribution to  $\mu_4$  is defined by the matrix element

$$f_2 M^2 S^\mu = \frac{1}{2} \sum_q e_q^2 \langle N | g \bar{\psi}_i \tilde{F}^{\mu\nu} \gamma_\nu \psi_i | N \rangle \quad (29)$$

where  $\tilde{F}^{\mu\nu}$  is the dual gluon-field strength tensor. A (generalized) definition of  $f_2$  in terms of the structure functions is

$$f_2(Q^2) = \frac{1}{2} \int_0^1 dx x^2 (7g_1(x, Q^2) + 12g_2(x, Q^2) - 9g_3(x, Q^2)), \quad (30)$$

where  $g_3$  is a parity-violating spin structure function which can be accessed by measurement of unpolarized lepton scattering off a longitudinally polarized target or with neutrino scattering. With only  $g_1$  and  $g_2$  data available,  $f_2$  can be extracted through Eqs. (18) and (21) if the twist-6 or higher terms are not significant.

The twist-3 and 4 operators describe the response of the collective color electric and magnetic fields to the spin of the nucleon. Expressing these matrix elements in terms of the components of  $\tilde{F}^{\mu\nu}$  in the nucleon rest frame, one can relate  $d_2$  and  $f_2$  to color electric and magnetic polarizabilities. These are defined as<sup>27,28,29,30</sup>

$$\chi_E 2M^2 \vec{S} = \langle N | \vec{j}_a \times \vec{E}_a | N \rangle, \quad \chi_B 2M^2 \vec{S} = \langle N | j_a^0 \vec{B}_a | N \rangle, \quad (31)$$

where  $\vec{S}$  is the nucleon spin vector,  $j_a^\mu$  is the quark current,  $\vec{E}_a$  and  $\vec{B}_a$  are the color electric and magnetic fields, respectively. In terms of  $d_2$  and  $f_2$  the color polarizabilities can be expressed as

$$\chi_E = \frac{2}{3} (2d_2 + f_2), \quad \chi_B = \frac{1}{3} (4d_2 - f_2). \quad (32)$$

### 3. Summary of previous experimental situation

Before Jefferson Lab started running polarized beams and targets, most of the spin structure measurements of the nucleon were performed at high-energy facilities like CERN (EMC<sup>32</sup> and SMC<sup>33,34,35,36,37</sup>), DESY (HERMES<sup>38,39,40</sup>) and SLAC (E80<sup>41</sup>, E130<sup>42</sup>, E142<sup>43</sup>, E143<sup>44</sup>, E154<sup>45,46</sup>, E155<sup>47,48</sup> and E155x<sup>49</sup>). The measured  $g_1$  and  $g_2$  data were suitable for an analysis in terms of perturbative QCD. The impetus for performing these experiments on both the proton and the neutron was to test the Bjorken sum rule, a fundamental sum rule of QCD. After twenty-five years of active investigation this goal was accomplished with a test of this sum rule to better than 10%. The spin structure of the nucleon was unraveled in the same process. Among the highlights of this effort is the determination of the total spin content of the nucleon due to quarks,  $\Delta\Sigma$  (see Eq. (19)). It revealed the important role of the quark orbital angular momentum and gluon total angular momentum. The main results from this inclusive double spin asymmetry measurement program have led to new directions namely the quest for an experimental determination of the orbital angular momentum contribution<sup>52</sup> (e.g., with Deep Virtual Compton Scattering at Jefferson Lab and other facilities) and the gluon spin contribution (with COMPASS<sup>50</sup> and RHIC-spin<sup>51</sup> experiments). These efforts will be ongoing for the next decades.

#### 4. Description of the JLab experiments

The inclusive experiments described here took place in the fall of 1998 in JLab Halls A<sup>53</sup> and B<sup>54</sup>. The accelerator produces a CW electron beam of energy up to 6 GeV. In Hall A the experiment was performed using incident beam energies of 5.06, 4.24, 3.38, 2.58 1.72 and 0.86 GeV and a beam current up to 15  $\mu\text{A}$ . In Hall B, beam energies of 2.56 and 4.28 GeV and currents up to 2.5 nA were used. A beam polarization of about 0.70, as measured by Halls A and B Møller polarimeters, was obtained by illuminating a strained GaAs cathode with polarized laser light. Data taken with unpolarized targets show that the beam charge asymmetry and false asymmetries are under control.

##### 4.1. Hall A

A polarized high pressure ( $\sim 12$  atm.) gaseous  $^3\text{He}$  target<sup>55,56,57</sup> was used as an effective polarized neutron target in the experiment performed in Hall A. The target cell is made of two connected chambers. Rubidium atoms, confined by a thermal gradient to the upper spherical chamber, are polarized by optical pumping. The polarization is then transferred to  $^3\text{He}$  nuclei by spin-exchange collisions. The latter descend by diffusion and convection to the lower chamber, a 40 cm long tube of 2 cm diameter, where they interact with the beam. The spins are held in a given direction by a 2.5 mT uniform field. The average target polarization, monitored by NMR and EPR techniques<sup>55,56,57</sup>, was  $0.35 \pm 0.014$  and its direction could be oriented longitudinal or transverse to the beam direction. The measurement of cross sections in the two orthogonal directions allowed a direct extraction of  $g_1^{3He}$  and  $g_2^{3He}$ , or equivalently  $\sigma_{TT}$  and  $\sigma_{LT}$ , without the need of models or unpolarized data.

The beam energy was measured with two independent devices to a few  $10^{-4}$  precision<sup>53</sup>, while its current was monitored to better than 1%. The scattered electrons were detected by two High Resolution Spectrometers (HRS) of  $\simeq 6$  msr angular acceptance and  $\simeq 9\%$  relative momentum acceptance, pointing at a nominal  $15.5^\circ$  angle. The high luminosity of  $10^{36} \text{ cm}^{-2}\text{s}^{-1}$  allowed for statistically accurate data at numerous HRS momentum settings that covered the  $(Q^2, \nu)$  plane, as is necessary to form moments at fixed  $Q^2$ . The detector package consisted of vertical drift chambers (for momentum analysis and vertex reconstruction), scintillation counters (data acquisition trigger) and Čerenkov counters and lead-glass calorimeters (for particle identification (PID)). The  $\pi^-$  were sorted from  $e^-$  with an efficiency better than 99.9%. Both HRS spectrometers were used to double the statistics and constrain the systematic uncertainties, by comparing the cross sections extracted using each HRS. Acceptances and optical properties were studied with a multi-foil carbon target and sieve-slit collimators. Carbon elastic cross sections were measured with 2% accuracy.

The kinematic coverage spans from the elastic reaction to slightly beyond the resonance region. Data from the pion threshold to  $W = 2$  GeV were used to form neutron moments. Polarized  $^3\text{He}$  elastic data were used to cross-check target and



beam polarimetry at the 4% level and absolute cross sections at the 5 – 7% level. Electromagnetic radiative corrections were performed using the method of Mo and Tsai<sup>58</sup> for external radiative corrections, while internal radiative corrections were evaluated with a modified version of the POLRAD code<sup>59</sup> including new quasi-elastic and resonance data. The relative uncertainty on the radiative corrections was typically less than 20%. Other systematic uncertainties came from absolute cross-section measurements (5%), beam and target polarizations (both relative 4%).

The spin structure functions  $g_1^n$  and  $g_2^n$  are extracted using polarized cross-section differences in which contributions from unpolarized materials such as target windows, nitrogen or the two protons of the  $^3\text{He}$  nucleus cancel. Corrections for the two protons in  $^3\text{He}$  are still needed since they are slightly polarized due to the D state ( $\sim 8\%$ ) and S' state ( $\sim 1.5\%$ ) of the  $^3\text{He}$  wave function<sup>60</sup>. Corrections for binding and Fermi motion are also applied via a PWIA-based model<sup>60</sup>. The uncertainty on this correction varies from 10% at the lowest  $Q^2$  to  $< 5\%$  at larger  $Q^2$ . To form the neutron moments, the integrands (e.g.  $\sigma_{TT}$  or  $g_1$ ) are needed at constant  $Q^2$ . Six equally spaced values of  $Q^2$  were chosen in the range  $0.1 \leq Q^2 \leq 0.9 \text{ GeV}^2$  and the integrands were determined from the measured points by interpolation. To complete the moments for the unmeasured high-energy region, the Bianchi and Thomas parameterization<sup>70</sup> was used for  $4 < W^2 < 1000 \text{ GeV}^2$  and a Regge-type parameterization was used for  $W^2 > 1000 \text{ GeV}^2$ .

#### 4.2. Hall B

Polarized solid  $^{15}\text{NH}_3$  and  $^{15}\text{ND}_3$  targets<sup>63</sup> using dynamic nuclear polarization<sup>61,62</sup> were used in Hall B. Polarizations varied from 70% to 40% for  $\text{NH}_3$  and 25% to 10% for  $\text{ND}_3$ . The target material was cooled to 1.2 K and the spins were oriented by a longitudinal 5 T field.

The beam was rastered to evenly spread depolarization effects. The beam energy was obtained from Hall A measurements. Its current was monitored by a Faraday cup downstream of the target. The luminosity reached  $10^{33} \text{ cm}^{-2} \text{ s}^{-1}$ . The CEBAF Large Acceptance Spectrometer (CLAS) has a large angular ( $2.5\pi \text{ sr}$ ) and momentum acceptance, which is ideal for studying the  $Q^2$  evolution of moments. CLAS contains six superconducting coils that produce a toroidal magnetic field. Particles are characterized by three layers of drift chambers (tracking, momentum and charge information), a layer of scintillator paddles (time of flight), and Čerenkov counters supplemented by electromagnetic calorimeters (PID). After PID, the remaining  $\pi^-$  contamination was less than 1% of the electron rate. To cover lower angles and momenta, the target was shifted 55 cm upstream of its nominal location. The polar angle ranged from  $8^\circ$  to  $50^\circ$ . The azimuthal angular acceptance was about 80%. The lowest momentum accepted was 0.35 GeV for the proton run. The deuteron data were taken with in-bending torus field only, which yields a minimum angle of  $14^\circ$  and a minimum momentum of 0.5 GeV.

Since cross sections are more difficult to measure in a large-acceptance spec-

trometer and  $F_2(x, Q^2)$  and  $R(x, Q^2)$  are relatively well known<sup>64,65</sup>, it is easier to extract  $g_1(x, Q^2)$  using asymmetry measurements<sup>44</sup>. The physics asymmetry  $A_{||}$  is related to the measured one:  $A_{raw} = A_{||}(P_b P_t DF)/C_N$ .  $C_N=0.98$  is the effect of the polarized valence proton of  $^{15}\text{N}$ ,  $P_b(P_t)$  is the beam (target) polarization.  $DF \simeq 0.15(0.2)$  for  $\text{NH}_3$  ( $\text{ND}_3$ ) is the dilution factor from  $^{15}\text{N}$ ,  $^4\text{He}$  and windows on the beam path.  $DF$  was estimated using data from a carbon target. Parameterizations of proton and neutron cross sections were used to account for the difference between  $^{15}\text{N}$  and  $^{12}\text{C}$  nuclei. Acceptance and detector inefficiency cancels out to first order in the asymmetry ratio. Acceptance cuts were chosen such that second-order corrections remain negligible. The radiative corrections to  $A_{||}$  were done using RCSLACPOL<sup>66</sup> based on the same formalism as POLRAD. The cross sections are parameterized using the NMC fit of the unpolarized structure-function data<sup>67</sup> and the polarized data from SLAC, CERN and HERMES<sup>1</sup>. The resonance contribution is estimated by the MAID<sup>17</sup> and the ‘‘AO’’<sup>68</sup> models. The radiative corrections account for 20% of the total systematic uncertainty on  $\Gamma_1$  at low  $Q^2$  and 5% at larger  $Q^2$ .

The same model was used to extract  $A_1$  and  $g_1$  from  $A_{||}$ .  $F_2^p(x, Q^2)$  and  $R^p(x, Q^2)$  were measured at SLAC<sup>65</sup> and JLab<sup>65</sup>. The DIS part of  $g_2$  is calculated using Eq.(27) while its resonance part is obtained from the MAID and ‘‘AO’’ models. The model-dependence dominates the systematic uncertainty on  $\Gamma_1$ , contributing to about 75% at low  $Q^2$  and 50% at larger  $Q^2$  for the proton and 50% in average for the deuteron. The model was also used to estimate the unmeasured high-energy part of  $\Gamma_1^{p,d}$ . Nuclear corrections were applied to  $\Gamma_1^d$  to extract  $\Gamma_1^n$  by accounting for the deuteron D-state:  $\Gamma_1^n = 2\Gamma_1^d/(1 - 1.5\omega_D) - \Gamma_1^p$ , with the D-state probability  $\omega_D \simeq 0.05$ .

## 5. Recent results from Jefferson Lab

### 5.1. Results of the generalized GDH sum for the neutron

Fig. 1 shows the extended GDH integrals  $I(Q^2)$  (open circles) for the neutron, which were extracted from JLab experiment E94-010 (Hall A)<sup>3</sup>, from pion threshold to  $W = 2.0$  GeV. The uncertainties, when visible, represent statistics only; the systematics are shown by the grey band. The solid squares include an estimate of the unmeasured high-energy part. The corresponding uncertainty is included in the systematic uncertainty band. These data indicate a smooth variation of  $I(Q^2)$  to increasingly negative values as  $Q^2$  varies from  $0.9 \text{ GeV}^2$  towards zero. The data are more negative than the MAID model calculation<sup>17</sup>. The calculation includes contributions to  $I(Q^2)$  for  $W \leq 2 \text{ GeV}$ , and should thus be compared with the open circles. At high  $Q^2$ , the data approach the HERMES<sup>39</sup> neutron results (extracted from  $^3\text{He}$ ), which spans the range  $1.28 \text{ GeV}^2 < Q^2 < 7.25 \text{ GeV}^2$ , but includes only the DIS part of the GDH integral. The GDH sum rule prediction,  $I(0) = -232.8 \mu\text{b}$ , is indicated on Fig. 1, along with extensions to  $Q^2 > 0$  using two  $\chi\text{PT}$  calculations,

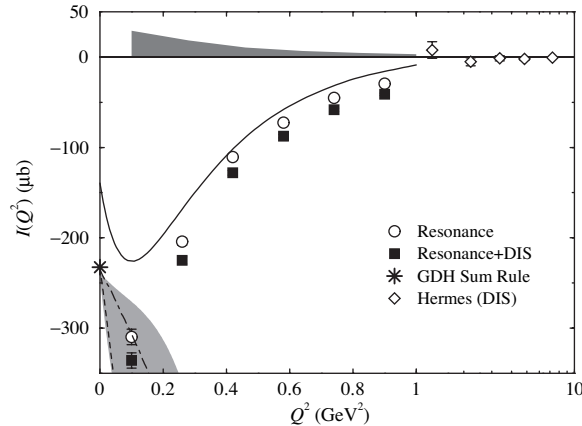


Fig. 1. Results for  $I(Q^2)$  are compared with  $\chi$ PT calculations of ref. <sup>71</sup> (dotted line) and ref. <sup>72</sup> (dot-dashed line). The MAID model calculation of ref. <sup>17</sup>, is shown with a solid line. Data from HERMES<sup>39</sup> are also shown and a log scale is used for  $Q^2 > 1 \text{ GeV}^2$ .

one using the Heavy Baryon approximation (HB $\chi$ PT) <sup>71</sup> (dotted line) and the other Relativistic Baryon  $\chi$ PT (RB $\chi$ PT) <sup>72</sup> (dot-dashed line). Shown with a grey band is RB $\chi$ PT including resonance effects <sup>73</sup>, which have an associated large uncertainty due to the resonance parameters used. The uncertainty can be seen to encompass both the lowest  $Q^2$  point and the calculation of Ref. <sup>71</sup>. At  $Q^2 = 0.3 \text{ GeV}^2$ , the prediction of Ref. <sup>72</sup> is much more negative than the data. Further calculations as well as further measurements<sup>a</sup> will help clarify the situation.

## 5.2. First moments of $g_1$ , $g_2$ and the Bjorken sum

Results on  $\bar{\Gamma}_1(Q^2)$  at low to moderate  $Q^2$  are available on the proton<sup>6</sup> and the neutron (using <sup>3</sup>He<sup>4</sup> and deuteron<sup>7</sup>). The integrals  $\bar{\Gamma}_1^p$ ,  $\bar{\Gamma}_1^n$ ,  $\bar{\Gamma}_2^n$  and  $\bar{\Gamma}_1^{p-n}$  are presented in Fig. 2 along with the data (open symbols) from SLAC<sup>43,44,45,47,49</sup> and HERMES<sup>38,40</sup>. The integral  $\bar{\Gamma}_1^p$  ( $\bar{\Gamma}_1^n$ ) was formed by summing  $g_1^p$  ( $g_1^n$ ) from pion threshold up to  $W = 2.6$  (2.0) GeV. Nuclear corrections were applied to the deuteron and <sup>3</sup>He data to extract  $\bar{\Gamma}_1^n$  as described in section 4. These results are shown by the open symbols. The sums including an estimation of the DIS contributions are shown by the solid symbols. The inner uncertainty indicates the statistical uncertainty while the outer one is the quadratic sum of the statistical and systematic uncertainties.

Data from the proton and neutron can be combined to form the flavor non-singlet moment  $\bar{\Gamma}_1^p(Q^2) - \bar{\Gamma}_1^n(Q^2)$  predicted in the Bjorken limit by the Bjorken sum rule<sup>2</sup>. It is generalized at large to moderate  $Q^2$  using OPE that yields a relatively

<sup>a</sup>JLab experiment E97-110, J.-P. Chen, A. Deur, and F. Garibaldi, spokespersons.

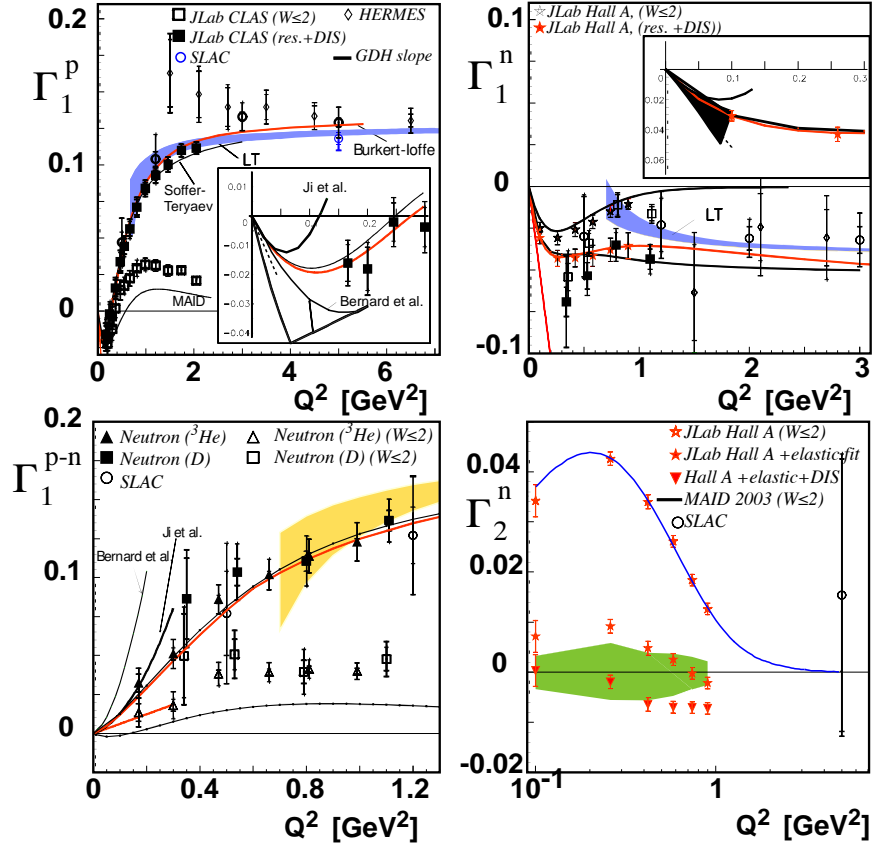
12 *J.-P. Chen, A. Deur and Z.-E. Meziani*


Fig. 2. Results for  $\overline{\Gamma}_1^p$  (top left),  $\overline{\Gamma}_1^n$  (top right) and the Bjorken sum (bottom left). The open circles (diamonds) represent the SLAC (HERMES) data. The open squares (stars) are the JLab CLAS (Hall A) data integrated over the resonance region, while the corresponding full symbols represent the full integrals. The slopes at  $Q^2=0$  predicted by the GDH sum rule are given by the dotted lines. The MAID model predictions that includes only resonance contributions are shown by the plain lines while the dashed (dot-dashed) lines are the predictions from the Soffer-Teryaev (Burkert-Ioffe) model. The leading twist (LT)  $Q^2$ -evolution of the moments is given by the grey band. The plain lines (bands) at low  $Q^2$  are the  $\chi$ PT predictions by Ji *et al.* (Bernard *et al.*).  $\Gamma_2^n$  is shown on the bottom right panel.

simple leading-twist  $Q^2$  evolution in which only non-singlet coefficients survive:

$$\int_0^1 (g_1^p - g_1^n) dx = \frac{g_a}{6} \left[ 1 - \frac{\alpha_s}{\pi} - 3.58 \left( \frac{\alpha_s}{\pi} \right)^2 - 20.21 \left( \frac{\alpha_s}{\pi} \right)^3 + \dots \right] + O\left(\frac{1}{Q^2}\right). \quad (33)$$

The Bjorken sum rule was verified to a level better than 10% at  $Q^2 = 5 \text{ GeV}^2$ .

Considering a flavor non-singlet object results in additional simplifications: the  $\Delta$  resonance contribution mostly cancels out so that  $\chi$ PT predictions are expected to be more reliable<sup>81</sup>, with possibly an extended domain of validity in  $Q^2$ . Furthermore, a flavor non-singlet moment is a convenient quantity for Lattice QCD calculations since disconnected diagrams, which are difficult to calculate, do not

contribute. Hence, the Bjorken sum is particularly suited to provide benchmark tests for the three theoretical frameworks used to study the transition from hadronic to partonic degrees of freedom.

To form  $\bar{\Gamma}_1^{p-n}$ , the proton and neutron data were re-analyzed at the same  $Q^2$  bins. The unmeasured low- $x$  part of the integral was re-evaluated for p, d and  $^3\text{He}$  data sets using a prescription described in section 4.1 with an additional constraint imposed by the Bjorken sum rule at  $Q^2 = 5 \text{ GeV}^2$ .

At  $Q^2=0$ , the GDH sum rule predicts the slopes of moments (dotted lines). The deviation from the slopes at low  $Q^2$  can be calculated with  $\chi\text{PT}$ . We show calculations by Ji *et al.*<sup>71</sup> using the HB $\chi\text{PT}$  and by Bernard *et al.* with<sup>73</sup> and without<sup>72</sup> including vector mesons and  $\Delta$  degrees of freedom (the band shows a range of results due to the uncertainty in the  $\gamma\text{N}\Delta$  form factor.) We do not show this result for the Bjorken sum because of the unknown correlation in the systematic uncertainties of the individual  $\bar{\Gamma}_1^p$  and  $\bar{\Gamma}_1^n$ . For the neutron this calculation overlaps with a data point at  $Q^2 = 0.1 \text{ GeV}^2$  while none of the  $\chi\text{PT}$  calculations agree with the proton data, of which the lowest  $Q^2$  point is  $0.17 \text{ GeV}^2$ . The calculation of Ji *et al.* agrees with the lowest  $Q^2$  data for the Bjorken sum. At moderate and large  $Q^2$  we show the MAID calculation<sup>17</sup>, to be compared with the data summed up to  $W = 2 \text{ GeV}$ . The model disagrees for  $\bar{\Gamma}_1^p$ ,  $\bar{\Gamma}_1^n$  and  $\bar{\Gamma}_1^{p-n}$ , with the wrong sign of the slope at the photon point for  $\bar{\Gamma}_1^{p-n}$  due to its underestimate of the GDH integral for the neutron at  $Q^2 = 0$ . The disagreement indicates that other contributions, not included in the model, are important.

The other calculations shown are by Soffer and Terayev<sup>74</sup> and by Burkert and Ioffe<sup>75</sup>. Those should be compared to the full experimental sum. The Soffer and Terayev model relies on the smooth  $Q^2$ -behavior of the  $I_T = I_1 + I_2$  integral to interpolate it between its known  $Q^2 = 0$  and large  $Q^2$  value.  $\bar{\Gamma}_1$  is extracted using the BC sum rule prediction on  $\bar{\Gamma}_2$ , Eq. (15). Power corrections and pQCD radiative corrections were recently added to the model to resolve the initial discrepancy with the JLab data. The Burkert and Ioffe model relies on a parameterization of resonances and non-resonance background<sup>68</sup> supplemented by a DIS parameterization based on vector meson dominance<sup>19</sup>. Both models agree well with the data.

The leading-twist pQCD evolution is shown by the grey band. For  $\bar{\Gamma}_1^{p(n)}$  we used  $\Delta\Sigma=0.15(\Delta\Sigma=0.35)$ ,  $a_s=0.579$  and  $g_a=1.267$  to anchor the evolution (see Eqs. (19) and (33)). The Bjorken sum rule sets the absolute scale for  $\bar{\Gamma}_1^{p-n}$ . In all cases, the leading twist tracks the data down to surprisingly low  $Q^2$ , which indicates an overall suppression of higher-twist effects. This is quantitatively discussed in section 5.4.

The capability of transverse polarization of the Hall A  $^3\text{He}$  target allows precise measurements of  $g_2$ . The integral  $\Gamma_2^n$  is extracted and plotted in the bottom-right panel of Fig. 2 in the measured region (open stars) and after adding the elastic contribution (solid stars)<sup>77</sup>. The solid triangles correspond to the results obtained after adding to the solid stars an estimated DIS contribution assuming  $g_2 = g_2^{WW}$ . The MAID estimate (solid line) agrees well with the resonance data. The positive light

grey band corresponds to the total experimental systematic errors. The negative dark band is the estimate of the systematic error for the low- $x$  extrapolation. The results (solid stars) are consistent with the BC sum rule to within 2 standard deviations over the measured  $Q^2$  range. The SLAC E155x collaboration<sup>49</sup> previously reported a neutron result at high  $Q^2$  (solid circle), where the elastic contribution is negligible; the result is consistent with zero but with a rather large error bar. On the other hand, the proton result was reported to deviate from the BC sum rule by 3 standard deviations. The quoted uncertainty in this case is 3 times smaller than that for the neutron, but still large.

### 5.3. Spin Polarizabilities: $\gamma_0$ , $\delta_{LT}$ and $d_2$ for the neutron

The generalized spin polarizabilities provide benchmark tests of  $\chi$ PT calculations at low  $Q^2$  and of Lattice QCD calculations at moderate to high  $Q^2$ . Since the generalized polarizabilities have an extra  $1/\nu^2$  weighting compared to the first moments (GDH sum or  $I_{LT}$ ), these integrals have less contribution from the large- $\nu$  region and converge much faster, which minimizes the uncertainty due to the unmeasured region at large  $\nu$ .

At low  $Q^2$ , the generalized polarizabilities have been evaluated with  $\chi$ PT calculations<sup>79,72</sup>. One issue in the  $\chi$ PT calculations is how to properly include the nucleon resonance contributions, especially the  $\Delta$  resonance, which usually dominates. As was pointed out in Ref. <sup>79,72</sup>, while  $\gamma_0$  is sensitive to resonances,  $\delta_{LT}$  is insensitive to the  $\Delta$  resonance. Measurements of the generalized spin polarizabilities are an important step in understanding the dynamics of QCD in the chiral perturbation region.

The first results for the neutron generalized forward spin polarizabilities  $\gamma_0(Q^2)$  and  $\delta_{LT}(Q^2)$  were obtained at Jefferson Lab Hall A<sup>5</sup> over a  $Q^2$  range from 0.1 to 0.9 GeV<sup>2</sup>. We will first focus on the low  $Q^2$  region where the comparison with  $\chi$ PT calculations is meaningful, and then show the complete data set. The results for  $\gamma_0(Q^2)$  are shown in the top-left panel of Fig. 3 for the two lowest  $Q^2$  values of 0.10 and 0.26 GeV<sup>2</sup>. The statistical uncertainties are smaller than the size of the symbols. The data are compared with a next-to-leading order,  $O(p^4)$ , HB $\chi$ PT calculation<sup>79</sup>, a next-to-leading-order RB $\chi$ PT calculation<sup>72</sup>, and the same calculation explicitly including both the  $\Delta$  resonance and vector meson contributions<sup>73</sup>. Predictions from the MAID model<sup>17</sup> are also shown. At the lowest  $Q^2$  point, the RB $\chi$ PT calculation including the resonance contributions is in good agreement with the experimental result. For the HB $\chi$ PT calculation without explicit resonance contributions, discrepancies are large even at  $Q^2 = 0.1$  GeV<sup>2</sup>. This might indicate the significance of the resonance contributions or a problem with the heavy baryon approximation at this  $Q^2$ . The higher  $Q^2$  data point is in good agreement with the MAID prediction, but the lowest data point at  $Q^2 = 0.1$  GeV<sup>2</sup> is significantly lower, consistent with what was observed for the generalized GDH integral result (Section 5.1). Since  $\delta_{LT}$  is insensitive to the dominating  $\Delta$  resonance contribution, it was believed that  $\delta_{LT}$

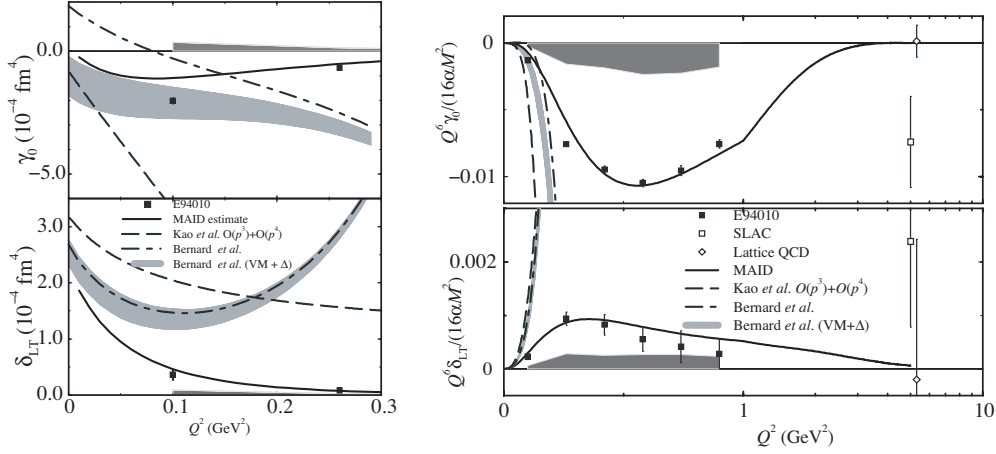


Fig. 3. Results for the neutron spin polarizabilities  $\gamma_0$  (top panels) and  $\delta_{LT}$  (bottom panels). Solid squares are the results with statistical uncertainties. The light bands are the systematic uncertainties. The dashed curves are the HB $\chi$ PT calculation<sup>79</sup>. The dot-dashed curves and the dark bands are the RB $\chi$ PT calculation<sup>72</sup>, without and with<sup>73</sup> the  $\Delta$  and vector meson contributions, respectively. Solid curves are from the MAID model<sup>17</sup>. The right panels are with  $Q^6$  weighting. The open squares are the SLAC data<sup>49</sup> and the open diamonds are the Lattice QCD calculations<sup>80</sup>.

should be more suitable than  $\gamma_0$  to serve as a testing ground for the chiral dynamics of QCD<sup>72,79</sup>. The bottom-left panel of Fig. 3 shows  $\delta_{LT}$  compared to  $\chi$ PT calculations and the MAID predictions. It is surprising to see that the data are in significant disagreement with the  $\chi$ PT calculations even at the lowest  $Q^2$ , 0.1  $\text{GeV}^2$ . This presents a significant challenge to the present theoretical understanding. The MAID predictions are in good agreement with the results.

The right panels of Fig. 3 show  $\gamma_0$  and  $\delta_{LT}$  multiplied by  $Q^6$  along with the MAID and  $\chi$ PT calculations. Also shown are the world data<sup>49</sup> and a quenched Lattice QCD calculation<sup>80</sup>, both at  $Q^2 = 5 \text{ GeV}^2$ . It is expected that at large  $Q^2$ , the  $Q^6$ -weighted spin polarizabilities become independent of  $Q^2$  (scaling)<sup>20,21</sup>, and the DIS Wandzura-Wilczek relation<sup>31</sup> leads to a relation between  $\gamma_0$  and  $\delta_{LT}$ :

$$\delta_{LT}(Q^2) \rightarrow \frac{1}{3}\gamma_0(Q^2) \quad \text{as } Q^2 \rightarrow \infty. \quad (34)$$

The results show that scaling is not observed for  $Q^2 < 1 \text{ GeV}^2$ . For the higher moments scaling is expected to start at a higher  $Q^2$  than for the first moments, for which scaling was observed to start around  $Q^2$  of 1  $\text{GeV}^2$ , where higher-twist effects become insignificant. Again, both results are in good agreement with the MAID model.

Another combination of the second moments,  $d_2(Q^2)$ , provides an efficient way to study the high  $Q^2$  behavior of the nucleon spin structure, since it is a matrix element, related to the color polarizabilities and can be calculated from Lattice QCD. It also provides a means to study the transition from high to low  $Q^2$ . In Fig. 4,  $\bar{d}_2(Q^2)$  is shown. The experimental results are the solid circles. The grey

band represents the systematic uncertainty. The world neutron results from<sup>49</sup> (open square) and from JLab E99-117<sup>83</sup> (solid square) are also shown. The solid line is the MAID calculation containing only the resonance contribution. At low  $Q^2$  the HB $\chi$ PT calculation<sup>79</sup> (dashed line) is shown. The RB $\chi$ PT<sup>72</sup> with or without the vector mesons and the  $\Delta$  contributions<sup>73</sup> are very close to the HB $\chi$ PT curve at this scale, and are not shown on the figure for clarity. The Lattice QCD prediction<sup>80</sup> at  $Q^2 = 5 \text{ GeV}^2$  is negative but close to zero. We note that all models (not shown at this scale) predict a negative or zero value at large  $Q^2$ . At moderate  $Q^2$ , our data show that  $\bar{d}_2^n$  is positive and decreases with  $Q^2$ .

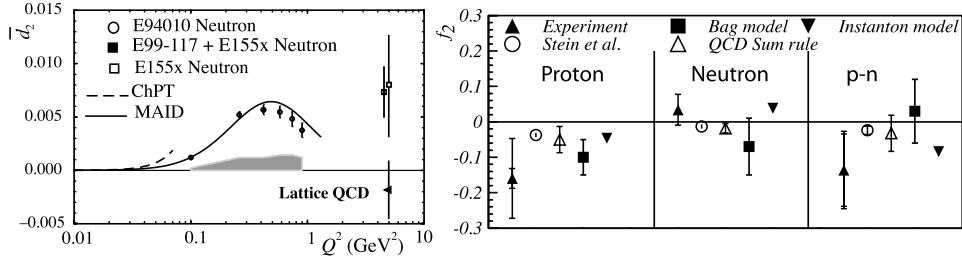


Fig. 4. The left panel shows the JLab results of  $\bar{d}_2$  for the neutron along with the world data at high  $Q^2$ , Lattice QCD, MAID model and HB $\chi$ PT calculations. The right plot compares  $f_2$  with calculations of Stein *et al.*<sup>28</sup>, MIT bag model<sup>30</sup>, QCD sum rules<sup>85</sup> and an instanton model<sup>86</sup>.

#### 5.4. Higher Twist extractions and $f_2$

The higher-twist contribution to  $\Gamma_1$  can be obtained by a fit with an OPE series, Eq. (18), truncated to an order appropriate for the precision of the data. The goal is to determine the twist-4 matrix element  $f_2$ . Once  $\mu_4$  is obtained,  $f_2$  is extracted by subtracting the leading-twist contributions of  $a_2$  and  $d_2$  following Eq. (21). To have an idea how the higher-twist terms (twist-8 and above) affect the twist-4 term extraction, it is necessary to study the convergence of the expansion and to choose the  $Q^2$  range in a region where  $\mu_8$  term is not significant. This study is made possible only with the availability of the new low- $Q^2$  data from JLab.

Higher-twist analyses have been performed on the proton<sup>10</sup>, the neutron<sup>8</sup> and the Bjorken sum<sup>11</sup>. An earlier proton analysis is available<sup>9</sup> but will not be presented here since it uses a different procedure.  $\Gamma_1$  at moderate  $Q^2$  is obtained as described in section 4. For consistency, the unmeasured low- $x$  parts of the JLab  $\Gamma_1^p$  and of the world data on  $\Gamma_1$  were re-evaluated using the same prescription previously used for  $\Gamma_1^n$  and  $\Gamma_1^{p-n}$ . The elastic contribution, negligible above  $Q^2$  of 2  $\text{GeV}^2$  but significant (especially for the proton) at lower values of  $Q^2$ , was added using the parametrization of Ref. <sup>77</sup>. The leading-twist term  $\mu_2$  was determined by fitting the data at  $Q^2 \geq 5 \text{ GeV}^2$  assuming that higher twists in this  $Q^2$  region are negligible. A value of  $g_A = 1.270 \pm 0.045$  was obtained for the Bjorken sum. Using the proton (neutron) data alone, and with input of  $g_A$  from the neutron beta decay and  $a_8$  from



the hyperon decay (assumed SU(3) flavor symmetry), we obtained  $\Delta\Sigma = 0.15 \pm 0.07$  for the proton and  $\Delta\Sigma = 0.35 \pm 0.08$  for the neutron. We note that there is a significant difference between  $\Delta\Sigma$  determined from the proton and from the neutron data. This is the main reason why the extracted  $\mu_4$  and  $f_2$  from the Bjorken sum is different compared to the difference of those extracted individually from the proton and neutron, since the Bjorken sum does not need the assumption of SU(3) flavor symmetry and  $\Delta\Sigma$  was cancelled.

The fit results using an expansion up to  $(1/Q^6)$  in determining  $\mu_4$  are summarized in Table 1. In order to extract  $f_2$ , shown in Table 2, the target-mass corrections  $a_2$  were evaluated using the Blumlein-Boettcher world data parametrization<sup>82</sup> for the proton and a world fit to the neutron data, which includes the recent high precision neutron results at large  $x$ <sup>83</sup>. The  $d_2$  values used are from SLAC E155x<sup>49</sup> (proton) and JLab E99-117<sup>83</sup> (neutron).

Table 1. Results of  $\mu_4$ ,  $\mu_6$  and  $\mu_8$  at  $Q^2 = 1 \text{ GeV}^2$  for proton, neutron and  $p-n$ . The uncertainties are first statistical then systematic.

Target	$Q^2 \text{ (GeV}^2\text{)}$	$\mu_4/M^2$	$\mu_6/M^4$	$\mu_8/M^6$
proton	0.6-11.0	$-0.065 \pm 0.012 \pm 0.048$	$0.143 \pm 0.021 \pm 0.056$	$-0.026 \pm 0.008 \pm 0.016$
neutron	0.5-11.0	$0.019 \pm 0.002 \pm 0.024$	$-0.019 \pm 0.002 \pm 0.017$	$0.00 \pm 0.00 \pm 0.03$
$p-n$	0.5-11.0	$-0.060 \pm 0.045 \pm 0.018$	$0.086 \pm 0.077 \pm 0.032$	$0.011 \pm 0.031 \pm 0.019$

Table 2. Results of  $f_2$ ,  $\chi_E$  and  $\chi_B$  at  $Q^2 = 1 \text{ GeV}^2$  for proton, neutron and  $p-n$ . The uncertainties are first statistical then systematic.

Target	$f_2$	$\chi_E$	$\chi_B$
$p$	$-0.160 \pm 0.028 \pm 0.109$	$-0.082 \pm 0.016 \pm 0.071$	$0.056 \pm 0.008 \pm 0.036$
$n$	$0.034 \pm 0.005 \pm 0.043$	$0.031 \pm 0.005 \pm 0.028$	$-0.003 \pm 0.004 \pm 0.014$
$p-n$	$-0.136 \pm 0.102 \pm 0.039$	$-0.100 \pm 0.068 \pm 0.028$	$0.036 \pm 0.034 \pm 0.017$

The  $\Gamma_1$  were fit, varying the minimum  $Q^2$  threshold to study the convergence of the OPE series. The extracted quantities have large uncertainties (dominated by the systematic uncertainty) but are stable with respect to the minimal  $Q^2$  threshold when it was below  $1 \text{ GeV}^2$ . The results do not vary significantly when the  $\mu_8$  term is added, which justifies *a posteriori* the use of the truncated OPE series in the chosen  $Q^2$  range. In the proton case, the elastic contribution makes a significant contribution to the  $\mu_6$  term at low  $Q^2$  but this does not invalidate *a priori* the validity of the series since the elastic contributes mainly to  $\mu_6$  and  $\mu_8$  remains small compared to  $\mu_4$ . We notice the alternation of signs between the coefficients. This leads to a partial suppression of the higher-twist effects and may be a reason for quark-hadron duality in the spin sector<sup>84</sup>. We also note that the sign alternation is opposite for the proton and neutron. The results are compared to theoretical calculations in Fig. 4. Following Eq. (32), the electric and magnetic color polarizabilities were determined. Overall, the values, given in Table 2, are small, and we observe a

sign change in the electric color polarizability between the proton and the neutron. We also expect a sign change in the color magnetic polarizability. However, with the large uncertainty and the small negative value of the neutron  $\chi_B$ , it is difficult to confirm this expectation.

## 6. Conclusion

A large body of nucleon spin-dependent cross-section and asymmetry data have been collected at low to moderate  $Q^2$  in the resonance region. These data have been used to evaluate the  $Q^2$  evolution of moments of the nucleon spin structure functions  $g_1$  and  $g_2$ , including the GDH integral, the Bjorken sum, the BC sum and the spin polarizabilities, and to extract higher-twist contributions. The latter provided access to the color polarizabilities in the nucleon.

At  $Q^2$  close to zero, available next-to-leading order  $\chi$ PT calculations were tested against the data and found to be in reasonable agreement for  $Q^2 = 0.1$  GeV<sup>2</sup> for the GDH integral  $I(Q^2)$ ,  $\Gamma_1(Q^2)$  and the forward spin polarizability  $\gamma_0(Q^2)$ . Above  $Q^2 = 0.1$  GeV<sup>2</sup> a significant difference between the calculation and the data is observed, pointing to the limit of applicability of  $\chi$ PT as  $Q^2$  becomes larger. Although it was expected that the  $\chi$ PT calculation of  $\delta_{LT}$  would offer a faster convergence because of the absence of the  $\Delta$  contribution, the experimental data show otherwise. None of the available  $\chi$ PT calculations can reproduce  $\delta_{LT}$  at  $Q^2 = 0.1$  GeV<sup>2</sup>. This discrepancy presents a significant challenge to our theoretical understanding at its present level of approximations and might indicate that higher order calculations are necessary.

Overall, the trend of the data is well described by phenomenological models. The dramatic  $Q^2$  evolution of  $I_{GDH}$  from high to low  $Q^2$  was observed as predicted by these models for both the proton and the neutron. This behavior is mainly determined by the relative strength and sign of the  $\Delta$  resonance compared to that of higher energy resonances and deep inelastic processes. This also shows that the current level of phenomenological understanding of the resonance spin structure using these moments as observables is reasonable.

The neutron BC sum rule is observed to be verified within uncertainties in the low  $Q^2$  range due to a cancellation between the resonance and the elastic contributions. The BC sum rule is expected to be valid at all  $Q^2$ . This test validates the assumptions going into the BC sum rule, which provides confidence in sum rules with similar assumptions.

In the  $Q^2$  region above 0.5 GeV<sup>2</sup> the first moment of  $g_1$  for the proton, neutron and the proton-neutron difference were re-evaluated using the world data and the same extrapolation method of the unmeasured regions for consistency. Then, in the framework of the OPE, the higher twist  $f_2$  and  $d_2$  matrix elements were extracted. The low  $Q^2$  data allowed us to gauge the convergence of the expansion used in this analysis. The extracted higher-twist (twist-4 and above) effects are not significant for  $Q^2$  above 1 GeV<sup>2</sup>. This fact may be related to the observation that quark-hadron

duality works reasonably well at  $Q^2$  above 1 GeV<sup>2</sup>.

Finally, the proton and neutron electric and magnetic color polarizabilities were determined by combining the twist-4 matrix element  $f_2$  and the twist-3 matrix element  $d_2$  from the world data. Our findings show a small and slightly positive value of  $\chi_E$  and a value of  $\chi_B$  close to zero for the neutron, while the proton has slightly larger values for both  $\chi_E$  and  $\chi_B$  but with opposite signs.

Overall, the new JLab data have provided valuable information on the transition between the non-perturbative to the perturbative regime of QCD. They form a precise data set for twist expansion analysis and a check of  $\chi$ PT calculations.

Future precision measurements<sup>b76</sup> of the  $g_1$  and  $g_2$  structure functions at  $Q^2 \approx 1 - 4$  GeV<sup>2</sup> will reduce the uncertainty in the extracted higher-twist coefficients and provide a benchmark test of Lattice QCD.

### Acknowledgments

Thanks to Kees de Jager, Ron Gilman and Vince Sulkosky for careful proof-reading. This work was supported by the U.S. Department of Energy (DOE). The South-eastern Universities Research Association operates the Thomas Jefferson National Accelerator Facility for the DOE under contract DE-AC05-84ER40150, Modification No. 175.

### References

1. see, *e.g.*, B. W. Filippone and X. Ji, Adv. Nucl. Phys. **26**, 1 (2001).
2. J. D. Bjorken, Phys. Rev. **148**, 1467 (1966).
3. M. Amarian *et al.*, Phys. Rev. Lett. **89**, 242301 (2002).
4. M. Amarian *et al.*, Phys. Rev. Lett. **92**, 022301 (2004).
5. M. Amarian *et al.*, Phys. Rev. Lett. **93**, 152301 (2004).
6. R. Fatemi *et al.*, Phys. Rev. Lett. **91**, 222002 (2003).
7. J. Yun *et al.*, Phys. Rev. **C 67**, 055204 (2003).
8. Z.-E. Meziani *et al.*, Phys. Lett. **B 613**, 148 (2005).
9. M. Osipenko *et al.*, Phys. Lett. **B 609**, 259 (2005).
10. A. Deur, nucl-exp/0508022.
11. A. Deur *et al.*, Phys. Rev. Lett. **93**, 212001 (2004).
12. S. B. Gerasimov, Sov. J. Nucl. Phys. **2**, 598 (1965)
13. S. D. Drell and A. C. Hearn, Phys. Rev. Lett. **16**, 908 (1966).
14. J. Ahrens *et al.* Phys. Rev. Lett. **87**, 022003 (2001).
15. H. Dutz *et al.*, Phys. Rev. Lett. **91**, 192001 (2003).
16. H. Dutz *et al.*, Phys. Rev. Lett. **93**, 032003 (2004).
17. D. Drechsel, S.S. Kamalov, and L. Tiator, Phys. Rev. **D 63**, 114010 (2001).
18. X. Ji and J. Osborne, J. of Phys. G **27**, 127 (2001).
19. M. Anselmino, B. L. Ioffe, and E. Leader, Sov. J. Nucl. Phys. **49**, 136 (1989).
20. D. Drechsel, B. Pasquini and M. Vanderhaeghen, Phys. Rep. **378**, 99 (2003).
21. D. Drechsel and L. Tiator, Ann. Rev. Nucl. Part. Sci. **54**, 69 (2004).

<sup>b</sup>JLab proposal PR03-107, S. Choi, X. Jiang, Z.-E., Meziani, spokespersons.

20 *J.-P. Chen, A. Deur and Z.-E. Meziani*

22. see, *e.g.*, J. D. Bjorken and S. D. Drell, “Relativistic Quantum Fields”, McGraw Hill, New York (1965).
23. F. E. Low, Phys. Rev. **96**, 1428 (1954).
24. K. Wilson, Phys. Rev. **179**, 1499 (1969).
25. H. Burkhardt and W. N. Cottingham, Ann. Phys. (N.Y.) **56**, 453 (1970).
26. J. Ellis and R. L. Jaffe, Phys. Rev. **D 9**, 1444 (1974); *ibid.*, **D 10**, 1669 (1974).
27. E. V. Shuryak and A. I. Vainshtein, *Nucl. Phys.* **B 201**, 141 (1982).
28. E. Stein, P. Gornicki, L. Mankiewicz and A. Schäfer, *Phys. Lett.* **B 353**, 107 (1995).
29. X. Ji and P. Unrau, Phys. Lett. **B 333**, 228 (1994).
30. X. Ji and W. Melnitchouk, Phys. Rev. **D 56**,1 (1997).
31. S. Wandzura and F. Wilczek, Phys. Lett. **B 72**, 195 (1977).
32. J. Ashman *et al.*, Phys. Lett. **B 206**, 364 (1988).
33. SMC collaboration: D. Adams *et al.*, Phys. Lett. **B 329**, 399 (1994).
34. SMC collaboration: D. Adams *et al.*, Phys. Lett. **B 357**, 248 (1995).
35. SMC collaboration: D. Adams *et al.*, Phys. Lett.**B 396**, 338 (1997).
36. SMC collaboration: D. Adeva *et al.*, Phys. Lett. **B 302**, 533 (1993).
37. SMC collaboration: D. Adeva *et al.*, Phys. Lett.**B 412**, 414 (1997).
38. K. Ackerstaff *et al.*, Phys. Lett. **B 404**, 383 (1997).
39. K. Ackerstaff *et al.*, Phys. Lett. **B 444**, 531 (1998).
40. A. Airapetian, *et al.*, Phys. Lett. **B 442**, 484 (1998).
41. M. J. Alguard *et al.*, Phys. Rev. Lett. **37**, 1261 (1976).
42. M. J. Alguard *et al.*, Phys. Rev. Lett. **41**, 70 (1976).
43. P. L. Anthony *et al.*, Phys. Rev. **D 54**, 6620 (1996).
44. K. Abe *et al.*, Phys. Rev. **D 58**,112003 (1998).
45. K. Abe *et al.*, Phys. Rev. Lett. **79**, 26 (1997).
46. K. Abe *et al.*, Phys. Lett. **B 404**, 377 (1997).
47. P. L. Anthony, *et al.*, Phys. Lett. **B 493**, 19 (2000).
48. P. L. Anthony, *et al.*, Phys. Lett. **B 458**, 529 (1999).
49. P. L. Anthony *et al.*, Phys. Lett. **B 553**, 18 (2003).
50. C. Bernet, Proceedings of DIS2005 (2005), Madison, Wisconsin, AIP Conf. Proc. (2005).
51. A. Deshpande, Proceedings of DIS2005 (2005), Madison, Wisconsin, AIP Conf. Proc. (2005).
52. X. Ji, Phys. Rev. Lett. **78**, 610 (1997).
53. Hall A collaboration: J. Alcorn *et al.*, Nucl. Inst. Meth. **A522**, 294 (2004).
54. CLAS collaboration: B. A. Mecking *et al.*, Nucl. Inst. Meth. **A503**, 513 (2003).
55. J.S. Jensen, Ph.D. Thesis, California Institute of Technology, 2000 (unpublished)
56. I. Kominis, Ph.D. Thesis, Princeton University, 2000 (unpublished).
57. Details of JLab E94-010 and relevant theses can be found at [www.jlab.org/e94010/](http://www.jlab.org/e94010/).
58. L.W. Mo and Y.S. Tsai, Rev. Mod. Phys. **41**, 205 (1969).
59. I.V Akushevich and N.M. Shumeiko, J. Phys. **G 20**, 513 (1994).
60. C. Ciofi degli Atti and S. Scopetta, Phys. Lett. **B 404**, 223 (1997).
61. A. Abragam and M. Goldman, Rep. Prog. Phys. **41** 396 (1978).
62. D.G. Crabb and W. Meyer, Annu. Rev. Nucl. Part. Sci. **47**, 67 (1997).
63. C. D. Keith *et al.*, Nucl. Inst. Meth. A **501**, 327 (2003).
64. L.W. Whitlow *et al.*, Phys. Lett. **B 250**, 193 (1990);
65. Y. Liang *et al.*, nucl-ex/0410027.
66. K. Abe *et al.*, Phys. Rev. **D 58** 112003 (1998).
67. M. Arneodo *et al.*, Phys. Lett. **B 364**, 107 (1995).
68. V. Burkert and Z. Li, Phys. Rev **D 47**, 46 (1993).

69. J. Soffer, Phys. Rev. Lett. **74**, 1292 (1995).
70. N. Bianchi and E. Thomas, Nucl. Phys. **B 82** (Proc. Suppl.), 256 (2000).
71. X. Ji, C. Kao, and J. Osborne, Phys. Lett. B **472**, 1 (2000).
72. V. Bernard, T. Hemmert and Ulf-G. Meissner, Phys. Lett. **B 545**, 105 (2002)
73. V. Bernard, T. Hemmert and Ulf-G. Meissner, Phys. Rev. **D 67**, 076008 (2003).
74. J. Soffer and O. V. Teryaev, Phys. Rev. **D 70**, 116004 (2004).
75. V. D. Burkert and B. L. Ioffe, Phys. Lett. **B 296**, 223 (1992).
76. The Science Driving the 12 GeV Upgrade of CEBAF,  
[http://www.jlab.org/div\\_dept/physics\\_division/GeV.html](http://www.jlab.org/div_dept/physics_division/GeV.html).
77. P. Mergell, Ulf-G. Meissner and D. Drechsel, Nucl. Phys. **A 596**, 367 (1996).
78. S. A. Kulagin and W. Melnitchouk (to be published), private communication.
79. C. W. Kao, T. Spitzenberg and M. Vanderhaeghen, Phys. Rev. **D 67**, 016001 (2003).
80. M. Gockeler *et al.*, Phys. Rev. **D 63**, 074506, (2001).
81. V. D. Burkert, Phys. Rev. **D 63**, 097904 (2001).
82. J. Blumlein and H. Boettcher, Nucl. Phys. **636**, 225 (2002).
83. X. Zheng *et al.* Phys. Rev. **C 70**, 065207 (2004).
84. W. Melnitchouk, R. Ent and C. Keppel, Phys. Rept. **406**, 127 (2005).
85. I.I. Balitsky, V. M. Braun and A.V. Kolesnichenko, Phys. Lett. **B 242**, 245 (1990).
86. N-Y. Lee, K. Goeke and C. Weiss, Phys. Rev. **D 65**, 054008 (2002).